

Deconvolution enhanced direction of arrival estimation using one- and three-component seismic arrays applied to ocean induced microseisms

M. Gal,¹ A.M. Reading,¹ S.P. Ellingsen,² K.D. Koper,³ R. Burlacu³ and S.J. Gibbons⁴

¹*School of Physical Sciences (Earth Sciences) and CODES Centre of Excellence in Ore Deposits, University of Tasmania, Hobart, Australia.*

E-mail: martin.gal@utas.edu.au

²*School of Physical Sciences (Mathematics and Physics), University of Tasmania, Hobart, Australia*

³*Department of Geology and Geophysics, University of Utah, Salt Lake City, UT 84112, USA*

⁴*NORSAR, P.O. Box 53, 2027 Kjeller, Norway*

Accepted 2016 April 12. Received 2016 April 6; in original form 2015 December 6

SUMMARY

Microseisms in the period of 2–10 s are generated in deep oceans and near coastal regions. It is common for microseisms from multiple sources to arrive at the same time at a given seismometer. It is therefore desirable to be able to measure multiple slowness vectors accurately. Popular ways to estimate the direction of arrival of ocean induced microseisms are the conventional (fk) or adaptive (Capon) beamformer. These techniques give robust estimates, but are limited in their resolution capabilities and hence do not always detect all arrivals. One of the limiting factors in determining direction of arrival with seismic arrays is the array response, which can strongly influence the estimation of weaker sources. In this work, we aim to improve the resolution for weaker sources and evaluate the performance of two deconvolution algorithms, Richardson–Lucy deconvolution and a new implementation of CLEAN-PSF. The algorithms are tested with three arrays of different aperture (ASAR, WRA and NORSAR) using 1 month of real data each and compared with the conventional approaches. We find an improvement over conventional methods from both algorithms and the best performance with CLEAN-PSF. We then extend the CLEAN-PSF framework to three components (3C) and evaluate 1 yr of data from the Pilbara Seismic Array in northwest Australia. The 3C CLEAN-PSF analysis is capable in resolving a previously undetected *Sn* phase.

Key words: Time-series analysis; Numerical solutions; Computational seismology.

1 INTRODUCTION

Two processes are responsible for the generation of ocean induced microseisms in the frequency range 0.05–2 Hz. Primary microseisms are generated by the interaction between ocean waves and the sloping ocean floor close to the coastline (Hasselmann 1963; Ardhuin *et al.* 2015). Secondary microseisms are generated by opposing ocean wave trains with slightly different wavenumber k (Longuet-Higgins 1950). Seismic waves induced by the secondary process are observed from the deep ocean (Gerstoft *et al.* 2008; Euler *et al.* 2014; Beucler *et al.* 2015) as well as coastal areas (Cesaro 1994; Essen 2003; Schulte-Pelkum *et al.* 2004; Bromirski *et al.* 2005; Chevrot *et al.* 2007; Behr *et al.* 2013; Reading *et al.* 2014).

In array-based microseisms studies, it is common to observe multiple wave arrivals from different backazimuths owing to the complex nature of the frequency-dependent ambient noise field (Brooks *et al.* 2009; Koper & Hawley 2010; Traer *et al.* 2012;

Gal *et al.* 2015). This poses increased requirements on the detection techniques compared to a single source. The analysis of the wavefield may be carried out with the conventional or adaptive beamformer (Kelly 1967; Capon 1969) that show robust estimates but also suffer from limited resolution capabilities (Krim & Viberg 1996; Shumway *et al.* 2008).

In the presence of a strong source, weaker arrivals can remain undetected or are overshadowed by the beam pattern of the strong source. A further difficulty arises if the array has a wide mainlobe or strong sidelobe, which results in a blurred power spectrum in the case of multiple wave arrivals from different backazimuths. To mitigate the effect of a blurred power spectrum, Nishida *et al.* (2008) applied Richardson–Lucy (RL) deconvolution (Richardson 1972; Lucy 1974), which deconvolves the array response function from an image in a maximum likelihood fashion to reduce blurring. A similar approach named CLEAN (Högbohm 1974), was designed in the field of radio astronomy to remove bright objects from the

measured sky brightness distribution to improve the sensitivity to weaker emission. CLEAN iteratively removes the power and beam pattern of the strongest source and replaces it with a ‘clean’ beam to give a sidelobe-free representation of the sky. The algorithm was adapted to acoustic beamforming as CLEAN-PSF (Sijtsma 2007), by iteratively removing fractions of plane wave energy from the cross-spectral density associated with the strongest source in the acoustic record. Hence, these techniques can be applied directly to seismic array data.

The increase of publicly available three-component (3C; one vertical and two horizontals) single station and array data allows for the study of the full seismic wavefield. For the single station case, polarisation analysis methods are commonly used to infer the particle motion and arrival direction (Vidale 1986; Park *et al.* 1987; Jurkevics 1988; Schimmel & Gallart 2003, 2004). In the case of ocean induced microseisms, the use of single station analysis provides a great alternative for regions with no seismic arrays (Schimmel *et al.* 2011; Sergeant *et al.* 2013; Davy *et al.* 2015). For 3C array data, beamforming can be performed separately for each component by rotation of the horizontal components (Poggi & Fäh 2010; Gibbons *et al.* 2011; Behr *et al.* 2013) or using all components simultaneously (Wagner 1996, 1997).

The aim of this work is to increase the resolution of the power spectrum to allow detection of weaker ocean induced microseisms and enable robust direction of arrival estimation. We evaluate the performance of RL deconvolution (Richardson 1972; Lucy 1974) and CLEAN-PSF (Sijtsma 2007) for three arrays (ASAR, WRA and NORSAR) with different apertures and compare the results with IAS Capon (Gal *et al.* 2014). We further extend the CLEAN-PSF algorithm to 3C seismic data. The performance of the 3C extension is assessed by evaluating 1 yr of data from the Pilbara Seismic Array (PSAR).

2 METHODS

2.1 Conventional beamforming

For the conventional Bartlett beamformer (Bartlett 1948), the sample cross-spectral matrix (also known as cross-power spectral density) is given as

$$\mathbf{C}(f) = \frac{1}{L} \sum_{l=1}^L \mathbf{X}_l(f) \mathbf{X}_l^\dagger(f) \quad (1)$$

where $\mathbf{X}_l(f)$ denotes the Fourier transform of the l th snapshot (temporal subwindow) $\mathbf{x}_l(t)$, \dagger is the conjugate transpose, f is the frequency and L the number of snapshots. Hence, the phase information for the wavefield at each seismic sensor, for a frequency f , is present in the cross-spectral matrix $\mathbf{C}(f)$. The power output of the beamformer is then

$$P(\mathbf{w}) = \mathbf{w}^\dagger \mathbf{C}(f) \mathbf{w} \quad (2)$$

where \mathbf{w} denotes a weight vector. For the conventional Bartlett beamformer, the weight vector is obtained by maximising the output power of the beamformer and it follows that

$$\mathbf{w}_B = \frac{\mathbf{a}(\mathbf{k})}{\sqrt{\mathbf{a}^\dagger(\mathbf{k})\mathbf{a}(\mathbf{k})}} \quad (3)$$

with $\mathbf{a}(\mathbf{k})$ denoting the steering vector and \mathbf{k} is the wavenumber. Inserting eq. (3) into eq. (2), leads to the power spectrum

$$P_B(\mathbf{k}) = \mathbf{w}_B^\dagger(\mathbf{k}) \mathbf{C}(f) \mathbf{w}_B(\mathbf{k}). \quad (4)$$

2.2 CLEAN and CLEAN-PSF algorithms

The CLEAN algorithm in its basic form, introduced in radio astronomy by Högbom (1974), is based on the assumption that the brightness distribution of the radio sky can be represented by spatially separated point sources. The idea is to find the position and strength of point sources and iteratively deconvolve their contribution to the image, that is, their point spread function (PSF). This iterative approach reduces the power of the ‘dirty’ image. Because the position and strength of the deconvolved source is known, point sources with the appropriate strength are placed into the ‘clean’ image. After a user specific threshold of source power was deconvolved (cleaning is stopped when the peak in the residual image reaches a level comparable with the theoretical noise), the ‘cleaned’ image is then constructed by convolving the clean components with an ideal beam (one with the same resolution as the array PSF, but no sidelobes) and adding the residual image. This approach is very successful in removing bright point objects that overshadow sources with a low signal-to-noise ratio (SNR).

Following the idea of CLEAN, the same principle of source power reduction can be introduced for conventional fk beamforming by removing the PSF (the point spread function is equivalent to array response function) from the power spectrum in a least-squares optimisation (Dougherty & Stoker 1998; Wang *et al.* 2004). CLEAN-PSF is an improved implementation of the conventional CLEAN that removes phase information associated with the strongest source directly from the cross-spectral matrix (Sijtsma 2007), hence mitigating edge effects for PSF’s that suffer from strong sidelobes. This extension allows the use of CLEAN-PSF with adaptive beamforming, that is, for slowness dependent PSF’s. CLEAN-PSF can be formulated by removing a fraction of the dominant source power $P_{B,\max}$ from the cross-spectral matrix

$$\mathbf{C}_{\text{PSF}}^{i+1} = \mathbf{C}^i - \phi P_{B,\max}^i \mathbf{w}_{\max} \mathbf{w}_{\max}^\dagger \quad (5)$$

where ϕ is the control parameter that determines the fraction of removed power and $\mathbf{w}_{\max}(\mathbf{k})$ is the normalised steering vector for a plane wave with a wavenumber \mathbf{k} that is associated with the maximum value in the power spectrum $P_{B,\max}^i(\mathbf{k})$. The idea behind removing a fraction of power is to iteratively remove sidelobe contributions associated with the strongest sources on the rest of the power spectrum. This process can be viewed as the introduction of a synthetic point source of negative power at the position of the dominant source. The choice of ϕ is in general data dependent and will be discussed on synthetic and observed data. Since the amount of removed power is known (e.g. $\phi = 0.05$ removes 5 per cent of power from the strongest source), we can construct the CLEAN power spectrum P_{CLEAN} as

$$P_{\text{CLEAN}}(\mathbf{k}) = \sum_i^M \phi P_{B,\max}^i \quad (6)$$

with M denoting the number of iterations and $\phi P_{B,\max}^i$ is the amount of reduced power for the dominant sources at iteration i . The final spectrum P_{PSF} is then obtained by summing the CLEAN and background spectrum

$$P_{\text{PSF}}(\mathbf{k}) = \mathbf{w}_B^\dagger(\mathbf{k}) \mathbf{C}_{\text{PSF}}^M(f) \mathbf{w}_B(\mathbf{k}) + P_{\text{CLEAN}}(\mathbf{k}), \quad (7)$$

where $\mathbf{C}_{\text{PSF}}^M(f)$ is the cross-spectral matrix after M iterations. The reason for adding the background spectrum is to obtain the correct power levels as phase information may be difficult to remove for high iterations once a low signal-to-noise ratio is present. The extension of CLEAN-PSF to the Capon beamformer follows a similar logic and is given in Appendix A. For our calculation, we use a nested grid

search to refine the position of the maximum in the slowness plane to an accuracy of 10^{-3} s deg $^{-1}$. This procedure is implemented to reduce error accumulation with increasing iteration number.

2.3 Richardson–Lucy algorithm

In astronomy and medical microscopy, a widely used method for the deblurring of images is the RL deconvolution (Richardson 1972; Lucy 1974). The data model of an observed image $I(x)$ is defined as

$$I(x) = P(x) * O(x) \quad (8)$$

where $P(x)$ denotes the PSF of the system, $O(x)$ is the original noise-free image, $*$ is the convolution operator and x denotes the image coordinates. Ideally, one wants to obtain the original noise-free image from the observed image and a known PSF. Richardson (1972) and Lucy (1974) addressed the reconstruction within a Bayesian framework that leads to the iterative equation

$$\hat{O}_{i+1}(x) = \hat{O}_i(x) \left[\frac{P(x)^T * \frac{I(x)}{P(x) * \hat{O}_i(x)}}{P(x)^T * \hat{O}_i(x)} \right], \quad (9)$$

where i denotes the iteration number and \hat{O}_0 is the first guess for the solution. This equation was later rederived as the maximum likelihood solution under Poisson statistics (Shepp & Vardi 1982). The equation therefore iteratively deconvolves the PSF under a maximum likelihood constraint. In this analysis, we use an implementation of RL deconvolution (Bertero & Boccacci 2005), previously successfully applied to beamforming (Nishida *et al.* 2008; Picozzi *et al.* 2010), that reduces Gibbs oscillations created by edge effects, allows the use of non-symmetric PSF's and improves overall performance.

The implementation is given as

$$\bar{O}_{i+1}(x) = \bar{w}(x) \bar{O}_i(x) \left[\frac{\bar{P}(x)^T * \frac{\bar{I}(x)}{\bar{P}(x) * \bar{O}_i(x) + b}}{\bar{P}(x)^T * \bar{O}_i(x) + b} \right], \quad (10)$$

where the bar denotes objects that have been extended by zero padding. The observed image $I(x)$ with a pixel length of $J \times J$ is extended by zero padding to the dimensions $2J \times 2J$ and placed into the centre of the extended area (an example of $\bar{I}(x)$ can be found in Fig. S1a). The same procedure is applied to $P(x)$, see Fig. S1b, and $O_i(x)$. The PSF placed into the centre of $\bar{P}(x)$ can have a larger extent than J and/or a non-symmetric form and is normalised to unity volume. The regularisation parameter b is the background noise level. When set, it will enforce the constrain of non-negativity upon the image. $\bar{w}(x)$ is defined as

$$\bar{w}(x) = \begin{cases} \frac{1}{\bar{\alpha}(x)} & \text{if } \bar{\alpha}(x) > \sigma \\ 0 & \text{otherwise} \end{cases} \quad (11)$$

with

$$\bar{\alpha}(x) = \bar{P}(x) * \bar{M}_s(x), \quad (12)$$

where $M_s(x)$ is a mask object of dimensions $J \times J$ filled with values equal to 1 and $\bar{M}_s(x)$ is the zero-padded version. Hence, $\bar{\alpha}(x)$ is the convolution of the zero-padded PSF with the mask object and describes the reach and influence of the PSF upon an image with dimensions $J \times J$. An example of both $\bar{\alpha}(x)$ and $\bar{w}(x)$ are shown in Fig. S1(c) and (d). The threshold parameter σ is introduced to avoid any divisions by zero during the iterative process and was suggested to be 0.01 or smaller for astronomical applications (Bertero & Boccacci 2005).

3 SYNTHETIC DATA

3.1 Point sources

We evaluate the performance of the two deconvolution approaches using synthetic data with the array element configurations of ASAR (aperture of 10 km), WRA (26 km) and NORSAR (77 km). Array locations, shapes, array response functions and relevant frequency bands are displayed in Fig. 1. We generate 10 synthetic sources with a phase velocity of 3.3 km s $^{-1}$ (simulating R_g waves) and 3 synthetic sources with a phase velocity of 4.1 km s $^{-1}$ (L_g waves), as shown in Fig. 2. The slowness distribution of the synthetic sources is chosen to cover a variety of scenarios, for example, multiple backazimuths, closely spaced sources and similar directions for R_g and L_g waves. Instead of creating synthetic seismograms and calculating the Fourier transform for each station to generate the cross-spectral matrix (eq. 1), we introduce phase shifts with equal power directly into the synthetic cross-spectral matrix

$$\mathbf{C}_{\text{syn}} = \sum_n \mathbf{w}_B(\mathbf{k}_n) \mathbf{w}_B^\dagger(\mathbf{k}_n), \quad (13)$$

where n iterates over the number of sources and $\mathbf{w}_B(\mathbf{k}_n)$ denotes the normalised steering vector of the n th source. For conventional (Bartlett) fk analysis in combination with CLEAN and RL, the cross-spectral matrix does not require additional processing prior to the beamforming procedure. In the case of the Capon method, we apply diagonal loading to ensure the existence of the inverse matrix (Featherstone 1997). In astronomy, the removed power is replaced by the mainlobe only. This could be done for the fk algorithm for which a mainlobe is data independent. For the Capon algorithm, the mainlobe is data dependent and varies in the slowness plane. We chose an arbitrary configuration, which is solely chosen for visualisation purposes and replace the removed power of sources in the CLEAN-PSF algorithm by a Gaussian kernel which occupies 7×7 gridpoints in the slowness plane and has no impact on the results. All other parameters used for the calculation are displayed in Table 1. The choice of the control parameter ϕ is selected in an accuracy versus computational cost compromise and will be discussed alongside the synthetic results. The iterations are stopped after a user defined value M , although other stopping criteria are discussed in Section 6. For the RL control parameter σ , we have tried a variety of threshold values and found robust estimates between $0.05 < \sigma < 0.11$.

The results of the synthetic analysis are displayed in Fig. 3. In the case of the conventional fk analysis, we find a blurred spectrum for each of the three arrays. Depending on the array station geometry and frequency band, each array shows unique resolution capabilities and shortcomings. The dense station configuration of ASAR shows good power suppression for faster arrivals (i.e. body waves), but strong blurring of surface waves due to the large beam mainlobe in the chosen frequency range (Fig. 1b). WRA shows strong aliasing due to its L-shaped geometry. NORSAR shows the best resolution of the three arrays for the surface waves. However, NORSAR with its seven dense subarrays (Fig. 1a) is prone to aliasing of body waves for the selected frequency range.

In the case of CLEAN-PSF, we find a strong improvement in source localisation for all three arrays and the recovery of previously overshadowed sources in the original power spectrum. In general, we see a suppression of artefacts generated by beam sidelobes, especially for the case of WRA and NORSAR. For the CLEAN-PSF with conventional fk, closely spaced sources are identified as a single source due to the overlapping array response. CLEAN-PSF

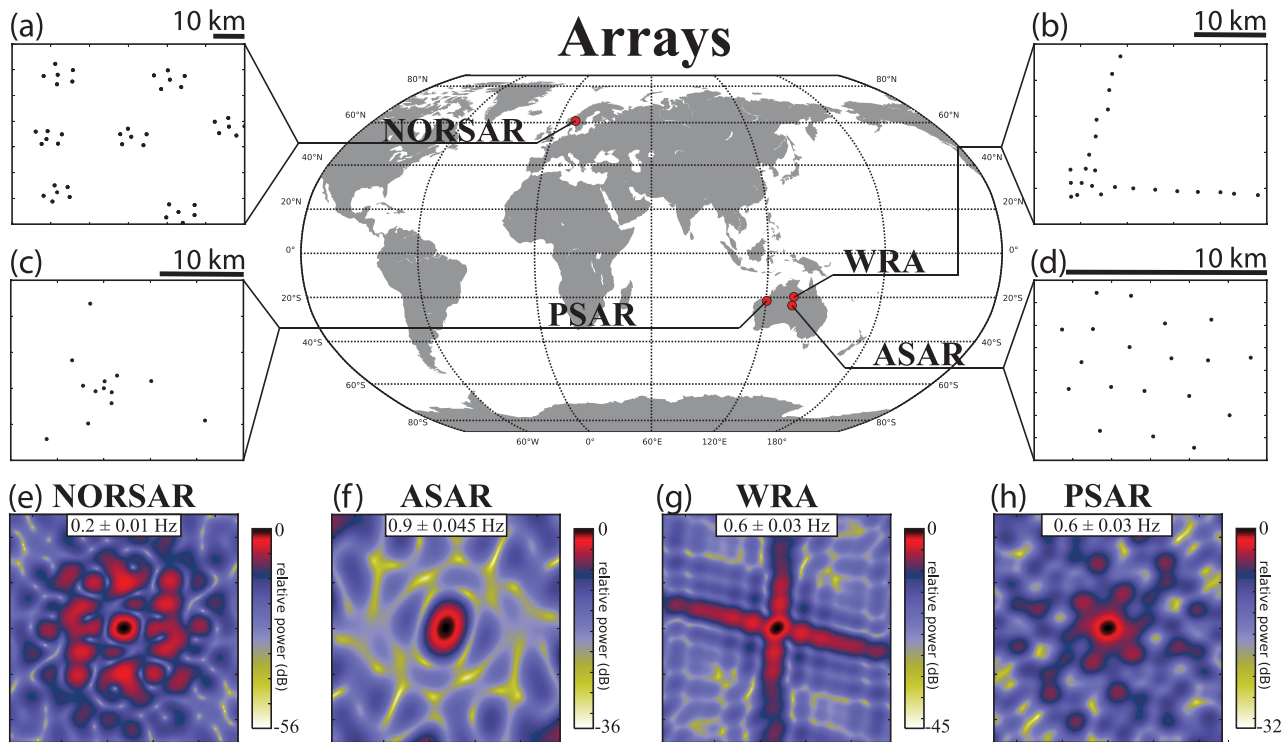


Figure 1. (a)–(d) Geographical location of the arrays with their station configurations and (e)–(h) array response functions. A scale of 10 km above each station configuration map is displayed as reference. The array response functions are displayed on a $\pm 50 \times \pm 50$ sdeg^{-1} slowness grid. The displayed frequencies are used during beamforming analysis of each array.

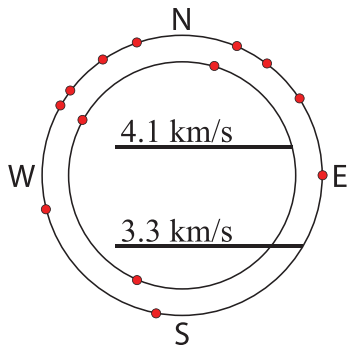


Figure 2. Representation of 10 synthetic sources with a velocity of 3.3 km s^{-1} and three synthetic sources with a velocity of 4.1 km s^{-1} in the slowness plane. All sources are generated with equal power.

in combination with Capon shows very good reconstruction of the true synthetic source parameters. Only minimal errors are visible for the case of ASAR, while WRA and NORARSAR show an error-free spectrum. We have tested a range of ϕ values and their influence on the recovery of weaker sources. In general, a small value of $\phi < 10^{-3}$ will converge towards a unique solution but suffers from high computational cost, that is, a high iteration number M . The optimal ϕ is dependent on the array design (number of stations and configuration), the frequency range chosen and the SNR. Arrays with a small station count and low SNR are likely to converge only for small ϕ values. For completeness, we display the convergence behaviour of CLEAN-PSF-fk for the ASAR case for different ϕ and iteration values and display which \tilde{k} is removed per iteration in Fig. S2.

The RL deconvolution shows strong reduction of blurring and a good recovery of synthetic sources for the case of ASAR and

Table 1. Parameters used for the analysis of synthetic and observed data. The following symbols denote: s_l snapshot length in seconds, n_w number of snapshots (windows), ϕ CLEAN control parameter, σ RL control parameter, M number of iterations where subscript C and RL are to be associated with the two deconvolution approaches and ‘stop’ denotes the stopping criterion for both algorithms.

	Array	s_l [s]	n_w	ϕ	σ	M	stop
Synthetic data							
Point sources	ASAR,WRA,NORSAR	∞	1	0.1	0.09	100 _C /200 _{RL}	User defined
Extended sources	ASAR,WRA,NORSAR	∞	1	0.1	0.09	180 _C /200 _{RL}	User defined
Observed data							
Single component	ASAR	100	71	0.05	0.09	120 _C /200 _{RL}	User defined
	WRA	200	35	0.05	0.09	120 _C /200 _{RL}	User defined
	NORSAR	400	17	0.05	0.09	120 _C /200 _{RL}	User defined
Earthquake excluded	ASAR	100	69	0.025	0.09	200 _C 200 _{RL}	User defined
Earthquake included	ASAR	100	71	0.025	0.09	250 _C /200 _{RL}	User defined
Three component	PSAR	200	35	0.1	-	60	User defined

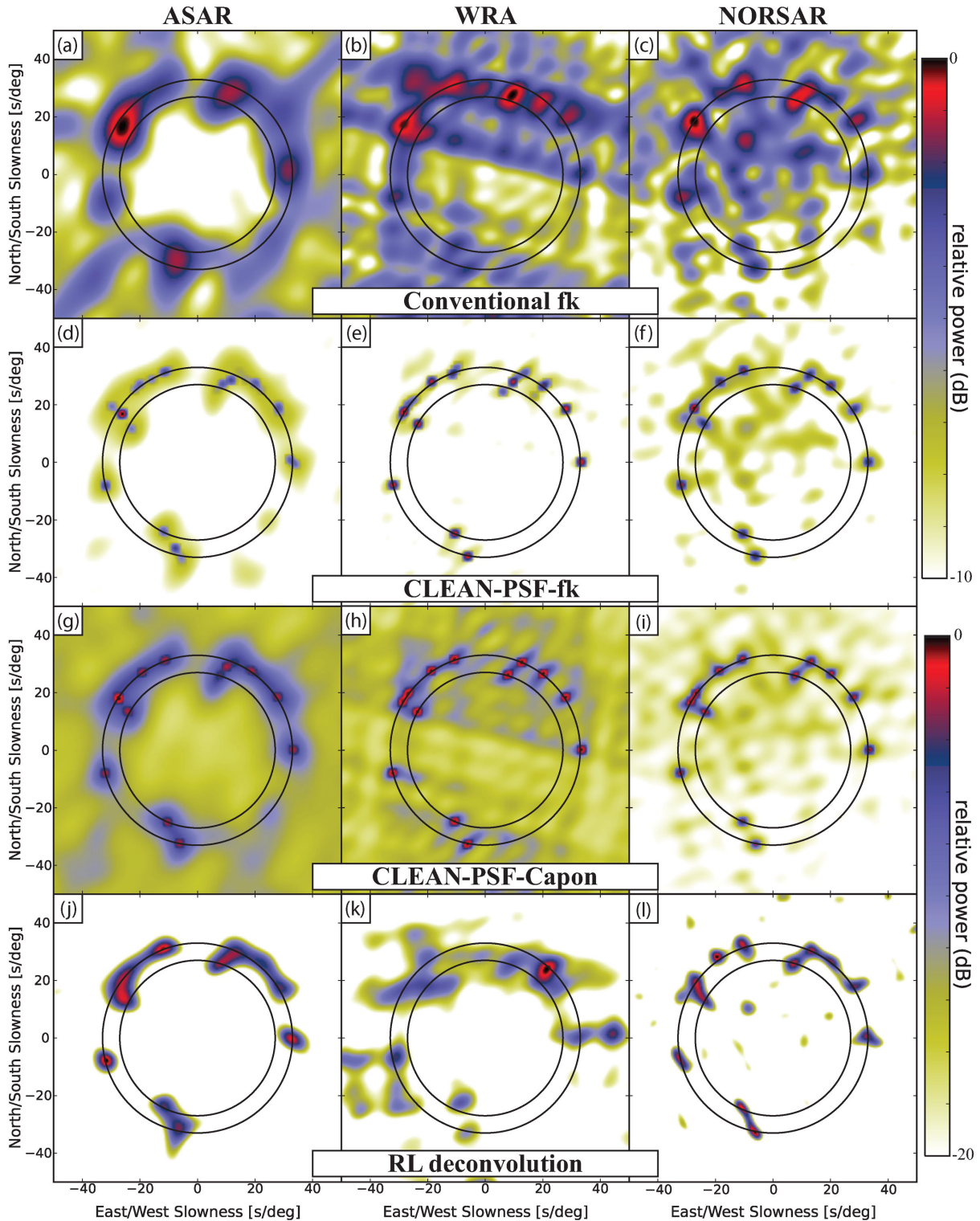


Figure 3. Comparison between different beamforming algorithms in the case of synthetic sources. Algorithms are displayed in rows, (a)–(c) conventional fk, (d)–(f) CLEAN-PSF with fk, (g)–(i) CLEAN-PSF with Capon and (j)–(l) RL deconvolution. Each column shows results from a specific array. Black circles of constant velocity are displayed at the true synthetic source velocities of 3.3 and 4.1 km s⁻¹.

NORSAR. For WRA, we see only minimal improvement in comparison with conventional fk. The reason for the low improvement is the PSF of WRA, which has relatively large sidelobes (Fig. 1g). In this specific case, better recovery can be obtained with a reflective boundary condition (Ng *et al.* 1999). In the conventional case pe-

riodic boundary conditions are used, while the reflective boundary acts as a mirror on the boundaries. To preserve consistency, we use the extension of Bertero & Boccacci (2005) for all further RL deconvolution calculations. It has to be noted that the RL deconvolution is strongly dependent on the number of iterations (Picozzi *et al.* 2010)

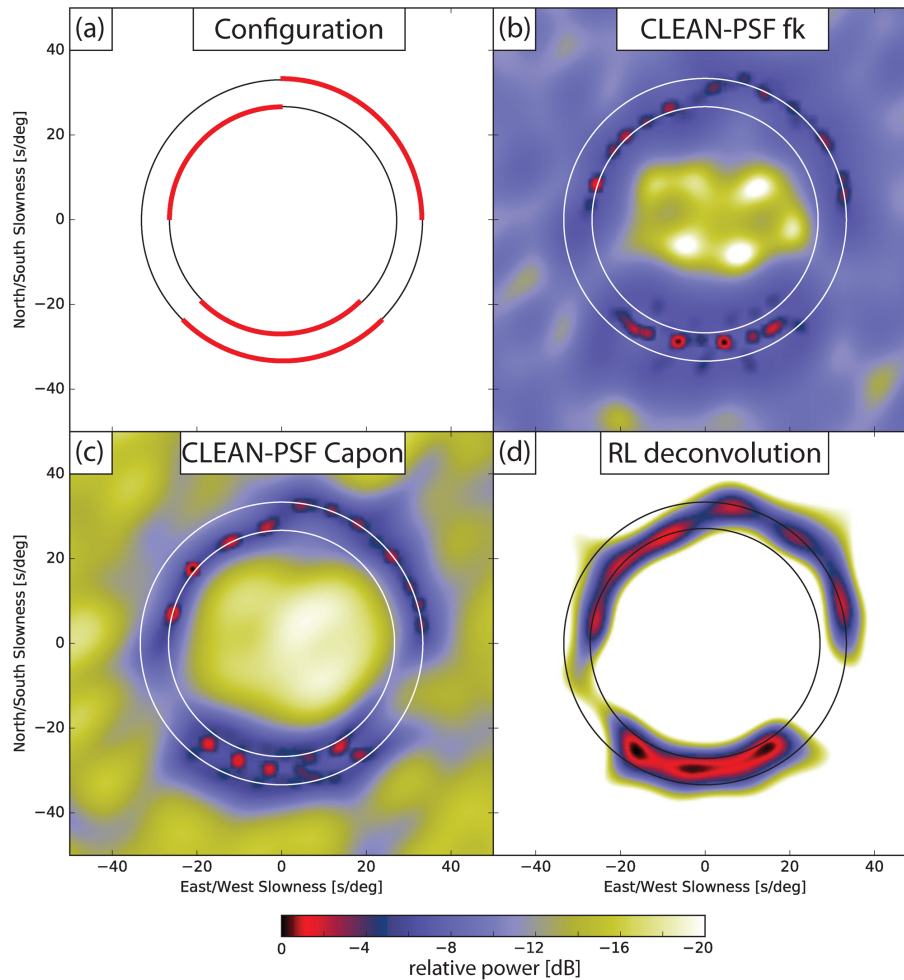


Figure 4. (a) Display of the synthetic configuration of extended sources. The red arcs symbolise incoming energy from extended backazimuths. The two black circles are placed at 3.3 and 4.1 km s^{-1} . Results for ASAR for the three approaches are shown in (b)–(d).

and the optimal number to achieve the best resolution/bias compromise requires an empirical approach. In this case, where the true source location of the synthetics is known, we chose the best match between the RL and the true power spectrum (200 iterations). We do not attempt to combine Capon beamforming with the RL approach, as the Capon power spectrum is not a superposition of PSFs, hence bias of weaker sources is to be expected.

The above results are presented with the idealisations of noise-free data and an infinite observation window. To account for noise and finite window effects, each source is constructed in the time domain with an SNR of -20 dB , a snapshot length of 200 s and the Hann window function is applied. The results are shown in Fig. S3 and display comparable results to the idealised case with minimal performance degradation for CLEAN-fk and RL while CLEAN-Capon suffers from the low SNR and shows worse source recovery than with the fk beamformer. Essentially, the deconvolution approaches are dependent on the performance of the underlying beamformer and are robust to noise in the study of ocean induced microseisms.

3.2 Extended sources

We simulate the performance of the deconvolution methods for the case of extended sources, see Fig. 4(a) for the synthetic configu-

ration. The results are presented for ASAR in Figs 4(b)–(d), while the results for WRA and NORSAR can be found in the Supporting Information, Fig. S4. Both CLEAN variations tend to cluster energy from extended backazimuths to a finite group of backazimuths for ASAR. The effect of clustering varies for all three arrays in this study and is less pronounced for WRA and NORSAR (Figs S4a,b,d and e). The clustering is dependent on the width of the mainlobe and the amount of recovered sources increases with a decreasing mainlobe width (e.g. WRA and NORSAR). The RL deconvolution shows a strong suppression of sidelobes and retains the structure of extended sources well for ASAR although little clustering is present as well. For NORSAR and WRA (Figs S4c and f), the RL deconvolution is not capable of resolving the extended sources. For NORSAR, we see strong artefacts in the centre of the slowness plane, which could not be removed due to the extended area of the PSF, while WRA shows a complete incompatibility for extended sources with RL deconvolution.

In conclusion, clustering can occur for the CLEAN approaches dependent on the PSF of the array, while the RL deconvolution retains a relatively smooth power output for arrays with a Gaussian PSF and shows strong performance degradation for extended (non-Gaussian type) PSFs. CLEAN further shows stronger resolution in the separation of closely spaced sources in the case of WRA and NORSAR, where the arrivals from the south are successfully resolved as waves with two distinct velocities.

4 OBSERVED DATA

In the following section, we evaluate the performance of the two algorithms on observed ambient noise data. The difference in aperture of the three arrays enables observations of different frequency bands within the microseism wavefield. The frequency bands of interest are 0.2 ± 0.01 Hz (NORSAR), 0.6 ± 0.03 Hz (WRA) and 0.9 ± 0.045 Hz (ASAR). We evaluate 1 month of observed data for ASAR (2010 January), WRA (2010 January) and NORSAR (2012 December).

Beamforming is performed on 1 hr data samples with conventional fk and Capon algorithms. Each 1 hr time-series is divided into smaller 50 per cent overlapping time windows (also known as snapshots) and tapered with the Hann window function to reduce spectral leakage. Each of these snapshots is Fourier transformed and used to construct a cross-spectral matrix that is an average of the 1 hr sample. The averaging over time increases the rank of the cross-spectral matrix and the robustness of the power spectrum. We additionally average over neighbouring frequencies with up to 5 per cent width of the projection (centre) frequency. The averaging over frequency further stabilises the power spectrum and allows us to evaluate a broader frequency range. It is important to keep the width over which frequency is averaged to a small percentage of the projection frequency as increasing the width leads to incorrect phase summation in the cross-spectral matrix (Menon *et al.* 2014; Gal *et al.* 2014). The main reason to apply averaging over frequency is that it gives rise to a well-structured cross-spectral matrix as phase information is extracted with the CLEAN algorithm. All other related parameters can be found in Table 1. For CLEAN, we chose $\phi = 0.05$ and $M = 120$ for all arrays which removes the following amount of relative power on average: ASAR = -3.5 dB, WRA = -4 dB and NORSAR = -6 dB. These values are chosen in order to be confident that the underlying beamformer is not degenerated by the SNR in the residual cross-spectral matrix. For the RL deconvolution, we choose the same parameters as in the synthetic case, as they seem to produce the best results for the observed data.

We compare the deconvolution approaches to IAS Capon (Gal *et al.* 2014) which has shown strong capabilities in estimating multiple wave arrivals from a variety of backazimuths. IAS Capon calculates multiple narrow-band spectra supported by diagonal loading to increase robustness of the solution. The narrow-band power spectra are combined to give a broad-band representation of the wavefield. For RL deconvolution, we use 200 iterations as this seems to yield the most reliable results in this case. The results are shown in Fig. 5. The summary plots are a combination of 1 hr evaluations for the whole month and are constructed by only considering local maxima above a certain relative power threshold (ASAR -3.5 dB, WRA -4 dB and NORSAR -6 dB), which is free of sidelobes due to CLEAN.

For ASAR (Fig. 5, left column), all four algorithms find multiple sources with a velocity of 3.3 km s^{-1} and 1–2 sources with a velocity of 4.1 km s^{-1} with identical backazimuths. IAS Capon shows the strongest contribution of artefact arrivals, which are caused by beam sidelobes of strong sources. This is to be expected as IAS Capon was not designed to recover weaker sources accurately (Fig. 5a, ~ 11.2 sources per hour). CLEAN-PSF removes these artefacts in both cases of fk and Capon, while Capon shows superior suppression capabilities, consistent with the synthetic tests. The RL algorithm shows a clean spectrum, but has the downside of recovering the least sources. We observe that the RL deconvolution does not preserve the power relations between sources and weaker sources are strongly

suppressed. Lowering the power threshold for ASAR below -3 dB shows an increase in weaker arrivals, but it is accompanied by an increase in artefacts with velocities $< 3 \text{ km s}^{-1}$.

For WRA (Fig. 5, middle column), we find most surface waves originate from the northern directions. IAS Capon shows signal concentrations along straight lines due to the array response. CLEAN-PSF-fk shows an improvement by reducing the presence of the array pattern although many scattered arrivals are visible. CLEAN-PSF-Capon displays the best performance in the suppression of the array pattern in both body and surface wave arrivals. With the RL deconvolution, we obtain a similarly bad resolution as in the synthetic case. The body wave arrivals do not match the results of the other three algorithms and very few sources are recovered overall. In the case of a reflective boundary condition, we observe an increase in source and artefact arrivals, hence little improvement.

NORSAR (Fig. 5, right column) shows arrivals from the Atlantic Ocean, in accordance with previous studies, for example, Friedrich *et al.* (1998). IAS Capon shows exceptional slowness vector recovery, as Rayleigh waves are estimated with a very sharp velocity profile (Fig. 5c). CLEAN-PSF-fk shows poorer performance, potentially due to the low sidelobe suppression of conventional fk. CLEAN-PSF-Capon shows a result similar to the IAS method with the exception of a body wave region (northwest), which is a likely artefact (we see a similar scenario for the synthetic case, where CLEAN-PSF-Capon suppresses an artificial body wave arrival, Fig. 3i). The RL deconvolution shows a result similar to CLEAN-PSF-Capon in suppression of artefacts, but recovers only half of the sources in comparison.

Overall, both CLEAN-PSF and RL deconvolution show an improvement in beam sidelobe reduction on ASAR and NORSAR, while CLEAN-PSF outperforms the RL deconvolution on WRA which has large sidelobes. CLEAN-PSF further shows a superior performance in weak source recovery on all three arrays.

4.1 Presence of an earthquake

Earthquakes are unwanted signals in the analysis of microseisms. Discarding earthquake perturbed data or performing a frequency normalisation to retain phase information only (e.g. Gerstoft *et al.* 2008), thus reducing the earthquake signal, are the common approaches. In the case of a strong earthquake, weaker microseism signals can remain undetected or their true slowness vector can be concealed due to the influence of strong beam sidelobes. We tested CLEAN-PSF and RL deconvolution on a 1 hr record of ASAR (2010 January 2, 00:00:00–01:00:00 UTC, magnitude: 5.1 mb, origin: Tonga Islands) to determine if the algorithms can accurately resolve weaker microseism sources in the presence of an earthquake. At first, we remove two snapshots that contain the earthquake signal and evaluate the noise wavefield. In the second step, we include the two snapshots containing the earthquake to study the influence of the strong arrival on the underlying noise wavefield. The results for the earthquake perturbed data set are displayed in Fig. 6.

The noise wavefield shows similar results for the two CLEAN variations and the RL deconvolution (Figs 6 a–c). Slight differences are visible for body waves and the southern direction where the CLEAN approaches indicate multiple arrivals while RL deconvolution estimates these arrivals as one source. With the included earthquake signal (Figs 6 d–f), both algorithms are capable of removing the array pattern from the earthquake source and show the same

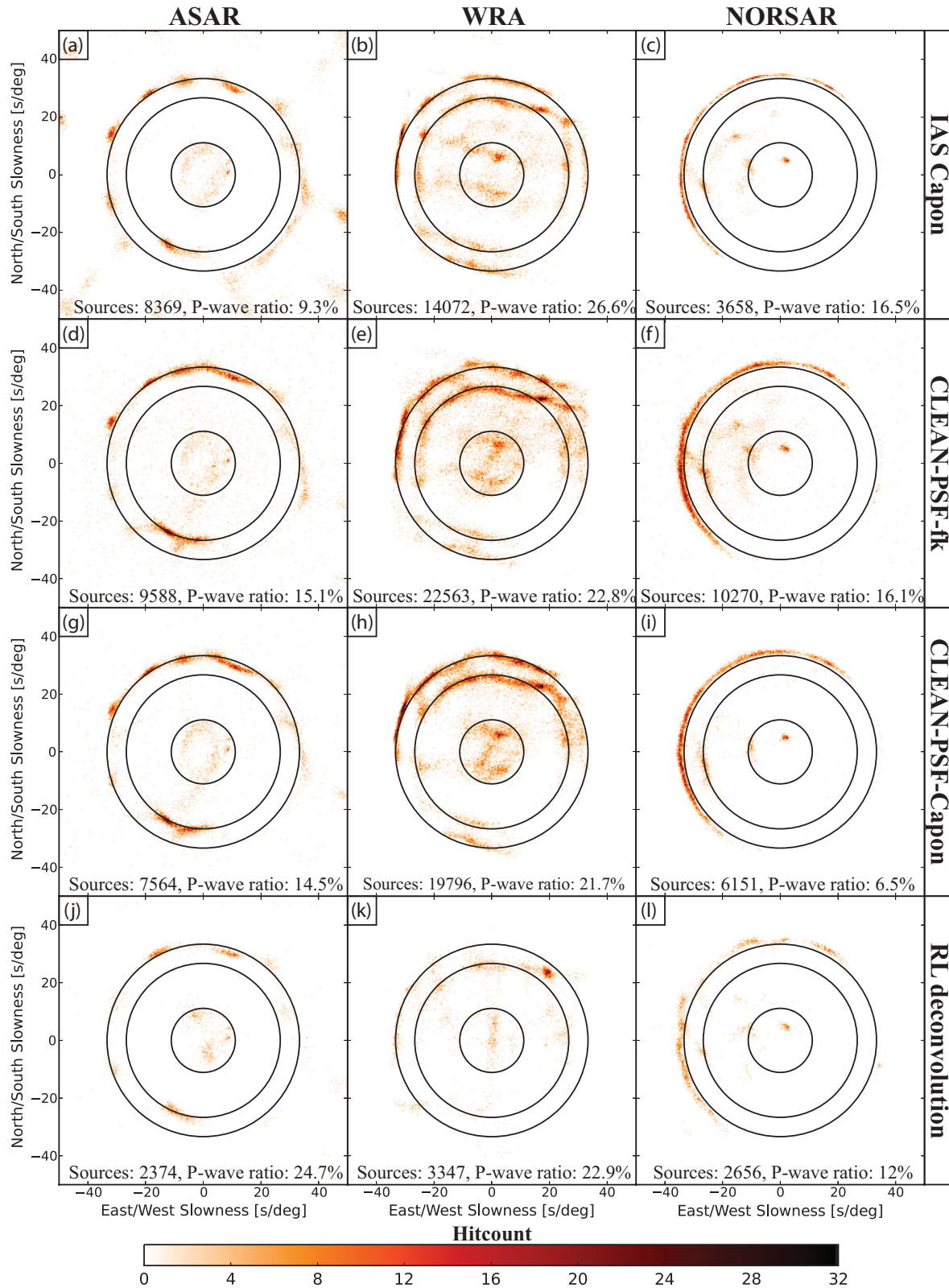


Figure 5. Beamforming summary (histograms) plots in the same layout as Fig. 3, but for observed array data. Instead of conventional fk, the first row shows beamforming results with IAS Capon. Circles of constant velocity are drawn at 3.3 and 4.1 km s⁻¹.

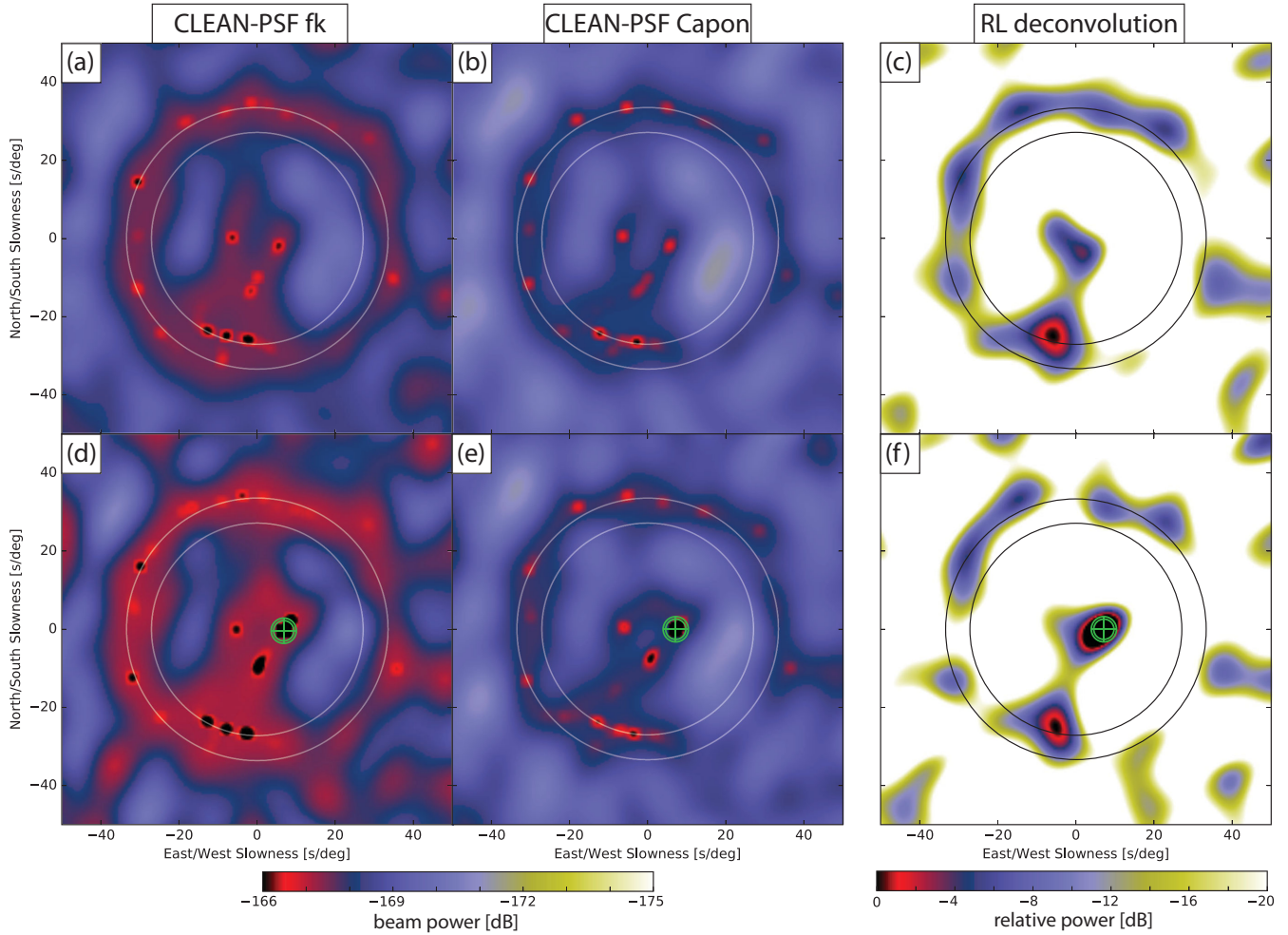


Figure 6. Beamforming results on a 1 hr long record of ASAR during an earthquake arrival. The top row shows the results which contain noise only. This was achieved by removing two snapshots from the cross-spectral matrix which contain the earthquake signal. The bottom row includes the earthquake signal which is marked with a green crosshair in the slowness plane. The algorithms are organised in columns, (a) and (d) CLEAN-PSF-fk, (b) and (e) CLEAN-PSF-Capon and (c) and (f) Richardson–Lucy deconvolution. Circles of constant velocity are set at 3.3 and 4.1 km s⁻¹. For the CLEAN approaches, we show the true beam power and clip the power of the earthquake arrival to show the background arrivals within the same limits. For the RL deconvolution, the results are shown with relative power, as RL does not accurately retain power information.

noise wavefield. For visualisation purposes, we clip the earthquake signal and show the same power levels as in the earthquake-free case, for an easy comparison of the noise wavefield. The results show that earthquake induced signals, including their sidelobe contributions, can be successfully removed from the power spectrum by both algorithms, while CLEAN-PSF shows higher resolution.

5 THREE-COMPONENT CASE

With the increasing deployment of seismic 3C arrays, better processing of 3C ground motion data is desirable. For 3C arrays, a popular way of performing the direction of arrival analysis is to rotate the horizontal north–south and east–west components into radial and transverse directions, for example, Fäh *et al.* (2008), Poggi & Fäh (2010), and Behr *et al.* (2013). Radial and transverse components are then processed separately, exploiting the fact that Rayleigh and Love waves have orthogonal particle motions. A disadvantage of this approach is that the cross-spectral matrix needs to be recalculated for each direction, and phase information between the three orthogonal directions are not recovered by this analysis.

5.1 Extension of CLEAN-PSF to 3C

We make use of an approach that evaluates all 3C simultaneously and allows access to polarisation information. The technique was developed by Wagner (1996) and can be used with multiple flavours of beamformers (fk, Capon, MUSIC and EMV). We briefly summarise the 3C approach followed by the extension of CLEAN for this framework. The 3C cross-spectral matrix is given as

$$\mathbf{C}_{3C}(f) = \frac{1}{L} \sum_{l=1}^L \mathbf{X}_{3C,l}(f) \mathbf{X}_{3C,l}^\dagger(f) \quad (14)$$

with

$$\mathbf{X}_{3C}(f) = [\mathbf{X}_{z1}, \dots, \mathbf{X}_{zK}, \mathbf{X}_{n1}, \dots, \mathbf{X}_{nK}, \mathbf{X}_{e1}, \dots, \mathbf{X}_{eK}]^T, \quad (15)$$

where \mathbf{X}_{ab} on the right-hand side denotes the Fourier transform of component a (vertical, north–south and east–west) and station b . Hence, $\mathbf{X}_{3C}(f)$ is a vector of length $3K$ and $\mathbf{C}_{3C}(f)$ is a $3K \times 3K$ matrix that governs the phase information between all 3C. The cross-spectral matrix is then projected onto the steering matrix composed of three orthogonal steering vectors

$$\mathbf{Y}_{3C}(\mathbf{k}) = \mathbf{e}^\dagger(\mathbf{k}) \mathbf{C}_{3C}(f) \mathbf{e}(\mathbf{k}) \quad (16)$$

with

$$\mathbf{e}(\mathbf{k}) = [\mathbf{a}_z(\mathbf{k}), \mathbf{a}_n(\mathbf{k}), \mathbf{a}_e(\mathbf{k})], \quad (17)$$

where the orthogonal $3K \times 3$ steering matrix $\mathbf{e}(\mathbf{k})$ is of the form

$$\mathbf{e}(\mathbf{k}) = \begin{bmatrix} a_{z1} & \dots & a_{zK} & 0 & \dots & 0 & 0 & \dots & 0 \\ 0 & \dots & 0 & a_{n1} & \dots & a_{nK} & 0 & \dots & 0 \\ 0 & \dots & 0 & 0 & \dots & 0 & a_{e1} & \dots & a_{eK} \end{bmatrix}^T \quad (18)$$

and $a_{zi} = a_{ni} = a_{ei}$ is the normalised steering vector from eq. (3). The resulting 3×3 polarisation covariance matrix $\mathbf{Y}_{3C}(\mathbf{k})$ is processed analogously to the single station case (Vidale 1986; Wagner & Owens 1996). An eigenvalue decomposition of $\mathbf{Y}_{3C}(\mathbf{k})$ transforms the polarisation characteristics into an orthogonal basis

$$\mathbf{Y}_{3C}(\mathbf{k}) = \mathbf{u}(\mathbf{k})\lambda(\mathbf{k})\mathbf{u}^\dagger(\mathbf{k}), \quad (19)$$

where the eigenvalues λ denote the strength for a certain polarisation direction that is given by the associated complex eigenvectors $\mathbf{u}(\mathbf{k})$. Each eigenvector parametrises the amplitude and phase relations of the 3C (z, n, e) for the given polarisation direction. The power estimate of the 3C conventional beamformer is the sum of the eigenvalues

$$P_{3C}(\mathbf{k}) = \lambda_0(\mathbf{k}) + \lambda_1(\mathbf{k}) + \lambda_2(\mathbf{k}). \quad (20)$$

The total power spectrum can be written as the sum of the 3C

$$\begin{aligned} P_{3C}(\mathbf{k}) &= \sum_{j=z,n,e} P_j(\mathbf{k}) = \sum_{j=z,n,e} \sum_{i=0}^2 \lambda_i(\mathbf{k}) |u_{i,j}(\mathbf{k})|^2 \\ &= \sum_{j=z,r,t} \tilde{P}_j(\mathbf{k}) = \sum_{j=z,r,t} \sum_{i=0}^2 \lambda_i(\mathbf{k}) |\tilde{u}_{i,j}(\mathbf{k})|^2, \end{aligned} \quad (21)$$

where tilde (e.g. $\tilde{P}_j(\mathbf{k})$) denotes rotated components from north–south, east–west to radial and transverse. For each wavenumber \mathbf{k} , that is, velocity, direction and frequency, the 3C beamformer yields an estimate of the amplitude and phase information of each component. The Capon 3C beamformer can be obtained by replacing the 3C cross-spectral matrix in eq. (16) by its inverse and inverting the eigenvalues

$$P_{3C, \text{Capon}}(\mathbf{k}) = \frac{1}{\lambda_0(\mathbf{k})} + \frac{1}{\lambda_1(\mathbf{k})} + \frac{1}{\lambda_2(\mathbf{k})}. \quad (22)$$

For strong transients and the case of conventional 3C beamforming, the largest eigenvalue λ_0 and eigenvector $\mathbf{u}_0(\mathbf{k})$ (assuming the eigenvalues and eigenvectors are sorted, $\lambda_0 > \lambda_1 > \lambda_2$) are used for the power estimate (e.g. Wagner 1997). This is a useful approach for signals whose polarisation characteristics can be described by a single eigenvalue/eigenvector pair, hence $\lambda_0 \gg \lambda_{1,2} \approx 0$. The remaining two eigenvalues are close to 0 and are dominated by noise. This approach is invalid for superimposed signals which are likely to occur in the study of ocean induced microseisms. We therefore outline the CLEAN approach in 3C in its general form for all three eigenvalues/eigenvectors.

The above framework allows us to implement the cleaning procedure in multiple ways. Signal removal can be performed on the maximum of the total power output, eq. (20), on each component (z, r, t) separately, or any other way appropriate for the user's application. We present the equations for CLEAN-PSF in 3C, where cleaning is subject to the maximal energy of the spectrum $\mathbf{P}_{3C}(\mathbf{k})$. In analogy to Section 2.2, the first step is to identify the dominant

contribution in the power spectrum, that is, $P_{3C, \text{max}}(\tilde{\mathbf{k}})$ along with its eigenvalues $\lambda_i(\tilde{\mathbf{k}})$ and eigenvectors $\mathbf{u}_i(\tilde{\mathbf{k}})$. We remove the power in 3C

$$\mathbf{C}_{3C}^{i+1} = \mathbf{C}_{3C}^i - \phi \sum_{j=0}^2 \lambda_j(\tilde{\mathbf{k}}) \mathbf{g}_j(\tilde{\mathbf{k}}) \mathbf{g}_j^\dagger(\tilde{\mathbf{k}}), \quad (23)$$

where

$$\mathbf{g}_j(\tilde{\mathbf{k}}) = \sum_{m=z,n,e} |u_{j,m}(\tilde{\mathbf{k}})| \mathbf{a}_m(\tilde{\mathbf{k}}) e^{i\psi_m(\tilde{\mathbf{k}})} \quad (24)$$

is a 1-D vector of length $3K$ constructed from the three orthogonal steering vectors $\mathbf{a}_m(\tilde{\mathbf{k}})$, see eqs (17) and (18). The vector $\mathbf{g}_j(\tilde{\mathbf{k}})$ essentially describes the componentwise plane wave propagation of all 3C associated with the strongest source in the power spectrum with the wave vector $\tilde{\mathbf{k}}$. The eigenvector $\mathbf{u}_0(\tilde{\mathbf{k}})$ assigns the contributions of each component, for example, for a Love wave $|u_{0z}(\tilde{\mathbf{k}})|$ will be close to 0, hence minimal power will be removed from the vertical z component. While the phase information is initially arbitrary (Vidale 1986), it is important to retain the phase information between the components, which we account for with $e^{i\psi_m(\tilde{\mathbf{k}})}$ for the m th component. This will ensure that polarisation properties are taken into account during the cleaning procedure (for instance, Rayleigh waves with a phase difference of 90° between the vertical and radial components).

Further calculations follow the same principals as CLEAN-PSF and the clean power spectrum is

$$P_{3C, \text{CLN}}(\mathbf{k}) = \sum_i^M \phi P_{3C, \text{max}}^i. \quad (25)$$

Combined with the background the full spectrum is of the form

$$P_{\text{PSF-3C}}(\mathbf{k}) = \mathbf{e}^\dagger(\mathbf{k}) \mathbf{C}_{\text{PSF}}^M(f) \mathbf{e}(\mathbf{k}) + P_{3C, \text{CLN}}(\mathbf{k}). \quad (26)$$

The CLEAN-PSF-3C approach can be combined with Capon beamforming following the same logic as in the 1-D case (see Appendix A).

In this work, we implemented CLEAN-PSF to clean each component separately, hence we computed three cross-spectral matrices (eq. 14) that are identical before CLEAN's first iteration. For the matrix $\mathbf{C}_{3C,i}$, we remove the energy associated with the local maxima from the i th component only. This approach will prevent the corruption of each component's power information. We illustrate the introduction of bias through the following example. Let there be three wave arrivals with equal strength (0 dB) and backazimuth, but different velocities (3.7, 4.4 and 5.6 km s⁻¹) and each wave is recorded by a separate component only. An illustration of the 3C fk beamformer output is displayed in the Supporting Information, Fig. S5 and the estimated parameters are given in Table S1. Even though the signals do not interfere with each other on any component, the polarisation analysis estimates power from the sidelobe contributions of the sources present on the other two components. This can be seen in the source present on the z component, which has power accurately estimated with 0 dB, while the other two components show a power of -2.22 dB, which is a result of sidelobes. Therefore, if a fraction of the power is removed from the z component, the other two components lose power proportional to their sidelobes power levels. This will bias the two other components and will inevitably lead to an incorrect decomposition of the spectrum. Hence, the easiest way to clean the components is to compute three cross-spectral matrices and clean each separately to obtain three unbiased components.

5.2 CLEAN-PSF-3C with observed data

For the 3C case, we use the PSAR which is comprised of 13 3C stations arranged in a spiral geometry (Kennett *et al.* 2015), located in northwest Australia. PSAR was deployed by Geoscience Australia and data access is available through the IRIS Data Management centre. The location, array configuration, array response and frequency band can be found in Fig. 1.

In the following section, we show the capabilities of CLEAN-PSF-3C by evaluating 1 yr of PSAR data (2013). Instead of conventional fk, we use the Capon beamformer in combination with the above framework. We average over time and frequency analogous to the vertical component case in Section 4. Since we are interested in the ambient noise field, and the main wave phases are R_g , L_g , P and Love waves (Nishida *et al.* 2008; Koper *et al.* 2010), we implement the CLEAN-PSF-3C algorithm to remove power separately from the strongest vertical, radial and transverse source per iteration (see Appendix B). We remove signals associated with the two smallest eigenvalues only (in the case of Capon the smallest eigenvalues represent the signals with strongest polarisation, see eq. 22), as the largest eigenvalue is, in general dominated by noise. All other parameters are stated in Table 1.

The results are presented in equivalent fashion to the single-component case as summary plots of the full year, for both 3C Capon beamforming and the CLEAN-PSF implementation (Fig. 7). We display local maxima up to a relative power threshold of -5 dB for each component, which is the amount that is cleaned on average by the CLEAN procedure. The first column shows the 3C Capon summary of arrivals for (1) vertical, (2) radial and (3) transverse components, respectively. A velocity histogram of the components is shown in Fig. 7(d). The second column (e)–(h) shows the corresponding CLEAN power spectra which were computed with 60 iterations. Increasing the number of iterations, hence removing less power in one step, leads to the same result.

The vertical and radial component plots (Figs 7a and b) are dominated by arrivals with a velocity of 3.3 km s^{-1} from the north to the west. For both components, these arrivals are found at identical positions in the slowness plane, hence show typical R_g behaviour. For arrivals from the south to the west, the positions in the slowness plane are not identical between the two components. This suggests an additional phase is present. A potential candidate is the L_g phase, as the vertical component shows arrivals with an increased velocity, in contrast to the radial component. The majority of body waves do not have correlated vertical and radial components and are hence likely to be artefacts. For the transverse component (Fig. 7c), we find a multitude of sources around a velocity of $3.9\text{--}4.0 \text{ km s}^{-1}$ present in the wavefield, which are likely Love waves.

Similarly, the CLEAN algorithm shows arrivals from the same directions on all 3C. For the cleaned vertical and radial components (Figs 7e and f), we find again identical positions in the slowness plane. In contrast to the conventional results, the cleaned spectrum shows significantly better resolution and is able to distinguish greater detail in arrivals from the main arrival directions in the north and west. Further, the previously scattered body waves are reduced and the remaining energy on the vertical and the radial component correlates well in the slowness plane. For the energy from the south to the west, little improvement is visible compared with the conventional approach. The cleaned transverse component shows additional sources from the northeast and southeast and reveals a previously undetected shear phase with a velocity around $4.6\text{--}4.7 \text{ km s}^{-1}$ (Fig. 7g). Comparing the two velocity histograms, Figs 7(d) and (h) illustrate the detection of this phase. A likely

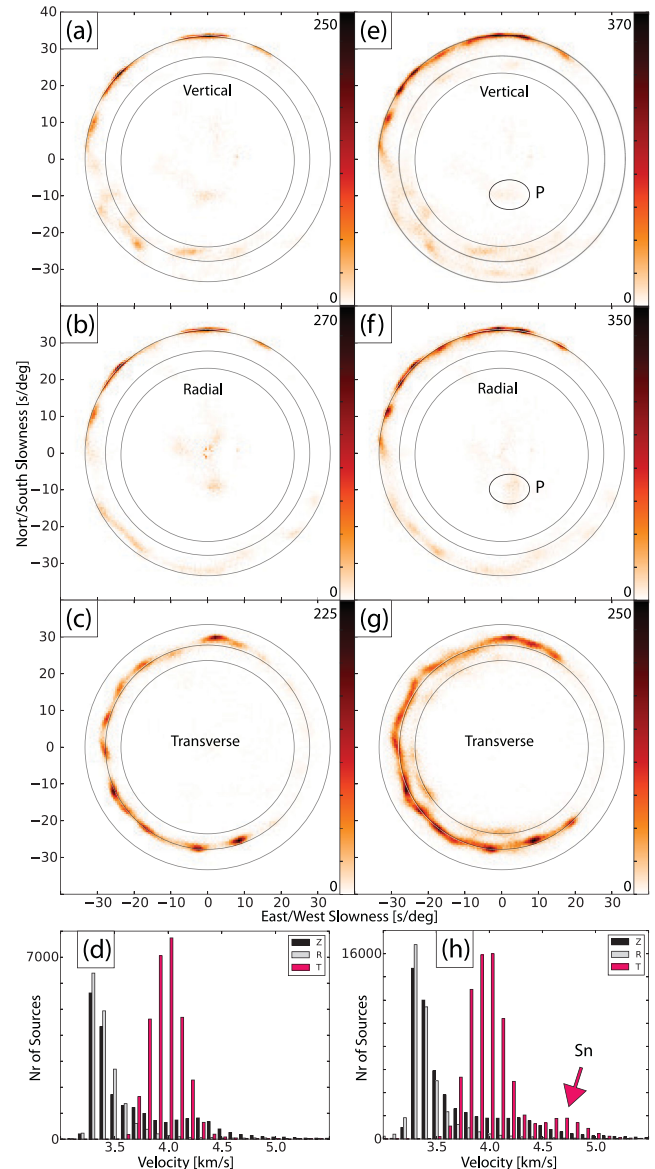


Figure 7. Beamforming summary plots (histograms) for (a)–(c) three-component Capon and (e)–(g) its CLEAN-PSF extension for each component. Circles of constant velocity are displayed at 3.3 , 4.0 and 4.7 km s^{-1} . The velocity histograms (d) and (h) were created from the arrival data in the corresponding column and display vertical, radial and transverse in black, white and red. For (e) and (f), we explicitly mark a region of P wave arrivals that correlate in the slowness plane.

candidate is the Sn phase, which matches the observed velocity in Australia (Huestis *et al.* 1973; Stephens & Isacks 1977).

6 DISCUSSION

For the single-component case, CLEAN-PSF shows significant resolution improvements in identifying weaker sources. The algorithm allows a specified amount of power to be cleaned from the spectrum and hence removes the associated sidelobe bias. Assuming the control parameter ϕ is not large, the algorithm converges to a solution. The extracted phases can be used to validate the accuracy of the solution by replacing the cross-spectral density matrix with the matrix that includes all removed phases (last term in eq. 5). This can be

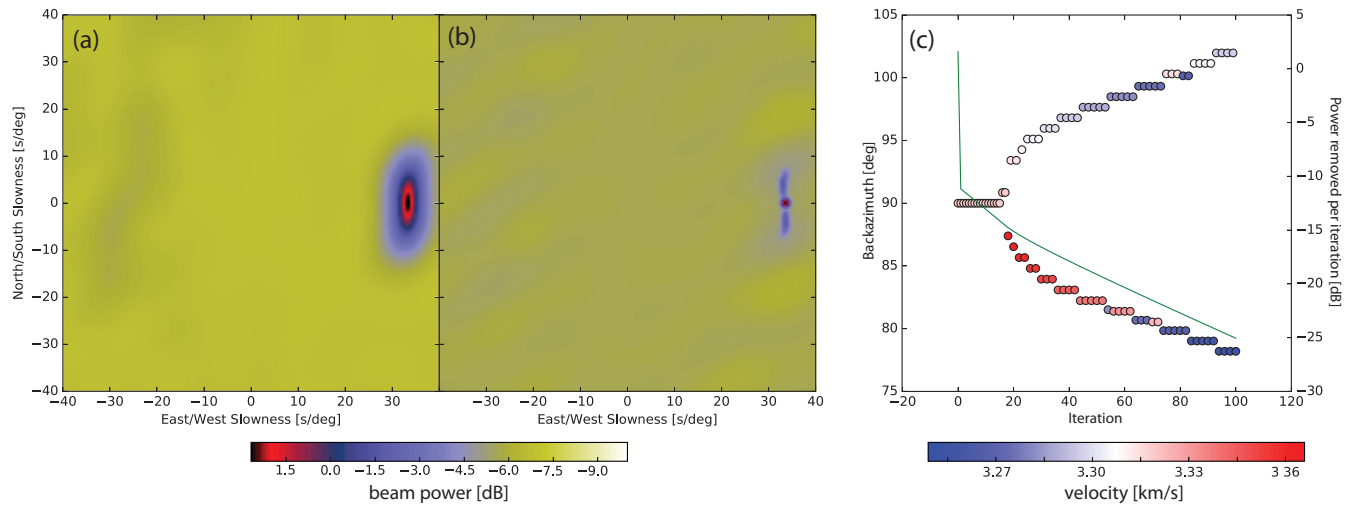


Figure 8. (a) Synthetic example of two closely spaced sources ($\text{baz} = 85^\circ$ and 95°), which cannot be separated by the Capon beamformer. (b) Displays the results after the CLEAN procedure. (c) Shows from which backazimuth power is removed as a function of the iteration and the green line marks the fraction of power removed as a function of iteration.

seen as a variation of the covariance fitting algorithm (Yardibi *et al.* 2008).

A limiting factor of CLEAN is its dependence on the dominant source. If the original beamformer result is biased in the dominant source, by a closely spaced source or multiple wave phases which generate an artificial local maximum due to sidelobe superposition, CLEAN will remove plane wave energy associated with the incorrect slowness vector and lead to an incorrect solution. A possible solution is to use a hybrid algorithm that combines CLEAN and RL deconvolution. Later iterations of CLEAN will benefit from a hybrid approach, as multiple peaks with the same power levels are likely to occur. Applying the RL algorithm in this scenario will give CLEAN a better estimate of the strongest source present in the spectrum, and therefore, enhance the correct recovery of weaker sources.

In contrast to CLEAN-PSF, the RL deconvolution does not depend on the position of the strongest source in the slowness plane and can in some cases correct the bias of the initial beamformer result. It shows strong deblurring capabilities but cannot resolve as many sources as CLEAN-PSF. A difficulty of the RL algorithm is the non-converging behaviour, hence it is strongly dependent on the number of iterations (Picozzi *et al.* 2010). It is not possible to find the optimal solution and a compromise between resolution and bias has to be selected by the user which limits the resolution capabilities of this approach.

In the conventional CLEAN in astronomy, the cleaning procedure is stopped once the maximum of the residual image reaches the level of the background noise. For beamforming, we have investigated two stopping criteria, apart from the trivial case in which the user sets the iteration number M to clean a specific amount of power. The first is to stop iteration after 1 eigenvalue of the covariance matrix becomes negative, that is, violates the positivity constraint embedded in the conventional beamformer. We found this approach to give unreliable results, owing to higher iterations lowering the SNR. This can strongly influence the performance of the underlying beamformer and CLEAN will remove random energy until the stop criterion is fulfilled. A more robust option is to monitor the parameters of the removed energy. In an iteration versus backazimuth plot, the removed energy tends to cluster around certain backazimuths (Fig. S2). Once the energy starts to scatter from these backazimuths,

it is likely that the underlying beamformer is biased by noise and CLEAN should be stopped. An illustrative figure is presented in the Supporting Information, Fig. S6.

The RL deconvolution faces the issue of a missing stop criterion in order to obtain the optimal solution. During our analysis, we find that the optimal number of iterations selected from synthetic tests, fits well with results from observed data for ASAR and NORSAR.

In the case of CLEAN, we examine the possibility of introducing errors by removing energy from the power spectrum that differs from the true source location. We study the behaviour for two closely spaced sources which cannot be separated by the underlying beamformer. Two noise-free synthetic sources are generated at backazimuth 85° and 95° and analysed with the ASAR configuration with CLEAN-Capon. In this case, we have set diagonal loading to a level where the two sources are observed as a single source by the Capon beamformer. Therefore, CLEAN will start to remove power between the two sources. The results shown in Fig. 8 display from which backazimuth power is removed, with each iteration. During the first iterations, power is removed from backazimuth 90° until enough power is removed to separate the two sources. The following iterations show that the removal of energy overshoots the true backazimuth values to compensate for the removal between the sources. The CLEAN approach cannot correctly separate the sources, but succeeds in the correct estimation of the combined power.

For completeness, we estimate the amplitude and slowness errors of the cleaned spectrum in the synthetic case presented in Section 3.1. The results are displayed in a backazimuth histogram for ASAR, WRA and NORSAR (Figs S7–S9). The estimated error in slowness depends on the wavefield and is greater when sources are closely spaced and cannot be separated by the beamformer and hence is dependent on the mainlobe of the array. For the case of ASAR, we find backazimuth errors of up to 5° and this decreases for the other arrays. The amplitudes are well estimated and show strong improvement over the conventional case (Fig. 3). For WRA and NORSAR the error in backazimuth is ($<3^\circ$) due to the increase in the number of stations and the smaller beam mainlobe.

The main source of error for the RL deconvolution is connected to the control/threshold parameter σ . In astronomy, the PSFs have a finite extent and can be easily normalised to unity volume. In array seismology, this is not the case as PSFs are not finite and can have

complicated shapes. This poses a problem as the volume of the PSF and σ are essentially dependent on the grid size of the PSF. The fact that the PSF is not finite is directly responsible that power levels of each source are not accurately estimated. We have tried a variety of threshold values and found robust estimates between $0.05 < \sigma < 0.11$ for ASAR and NORSAR. Between these two values, the RL deconvolution shows robust results when applied to synthetic data.

7 CONCLUSIONS

We have tested the performance of two deconvolution algorithms, CLEAN-PSF and RL deconvolution, in the context of a single-component array microseism (ambient noise) analysis. We used a range of arrays with different apertures and shapes (ASAR, WRA and NORSAR). In all three cases (synthetic, real and earthquake perturbed data), both approaches show improvement over the conventional methods in removing artefacts and identifying weaker sources. CLEAN-PSF shows better suppression capabilities mainly due to the fact that it can be used with the Capon beamformer. A further advantage was shown through an earthquake example, where CLEAN-PSF is capable of removing the earthquake imprint and revealing the underlying ambient noise sources.

We have extended the CLEAN approach to 3C and analysed its performance on 1 yr of 3C ambient noise data from PSAR. The extension demonstrates improved resolution on all 3C and reveals the previously undetected S_n phase. We therefore conclude that CLEAN-PSF is of strong utility in the study of the ambient noise field for the accurate identification of weaker arrivals for single- and three-component arrays.

ACKNOWLEDGEMENTS

We acknowledge data access through the IRIS DMC archive. Our thanks is due to two anonymous referees and the editor for constructive reviews which have improved both content and reproducibility. We further thank Hrvoje Tkalčić and Gregory Wagner for constructive discussions. The research was funded by the Australian Research Council (DP15101005) and MG supported through a Tasmanian Government Research Scholarship. Computer programs which implement the techniques are freely available and may be obtained by contacting the University of Tasmania authors.

REFERENCES

- Ardhuin, F., Gualtieri, L. & Stutzmann, E., 2015. How ocean waves rock the Earth: two mechanisms explain microseisms with periods 3 to 300 s, *Geophys. Res. Lett.*, **42**, 765–772.
- Bartlett, M.S., 1948. Smoothing periodograms from time-series with continuous spectra, *Nature*, **161**, 686–687.
- Behr, Y., Townend, J., Bowen, M., Carter, L., Gorman, R., Brooks, L. & Bannister, S., 2013. Source directionality of ambient seismic noise inferred from three-component beamforming, *J. geophys. Res.*, **118**, 240–248.
- Bertero, M. & Boccacci, P., 2005. A simple method for the reduction of boundary effects in the Richardson–Lucy approach to image deconvolution, *Astron. Astrophys.*, **437**(1), 369–374.
- Beucler, E., Mocquet, A., Schimmel, M., Chevrot, S., Quillard, O., Vergne, J. & Sylvander, M., 2015. Observation of deep water microseisms in the North Atlantic Ocean using tide modulations, *Geophys. Res. Lett.*, **42**(2), 316–322.
- Bromirski, P.D., Duennebieber, F.K. & Stephen, R.a., 2005. Mid-ocean microseisms, *Geochem. Geophys. Geosyst.*, **6**(4), doi:10.1029/2004GC000768.
- Brooks, L., Townend, J., Gerstoft, P., Bannister, S. & Carter, L., 2009. Fundamental and higher-mode Rayleigh wave characteristics of ambient seismic noise in New Zealand, *Geophys. Res. Lett.*, **36**(23), L23303, doi:10.1029/2009GL040434.
- Capon, J., 1969. High-resolution frequency–wavenumber spectrum analysis, *Proc. IEEE*, **57**(8), 1408–1418.
- Cessaro, R.K., 1994. Sources of primary and secondary microseisms, *Bull. seism. Soc. Am.*, **84**(1), 142–148.
- Chevrot, S., Sylvander, M., Benahmed, S., Ponsolles, C., Lefèvre, J.M. & Paradis, D., 2007. Source locations of secondary microseisms in western Europe: evidence for both coastal and pelagic sources, *J. geophys. Res.*, **112**(B11), B11301, doi:10.1029/2007JB005059.
- Davy, C., Stutzmann, E., Barruol, G., Fontaine, F. & Schimmel, M., 2015. Sources of secondary microseisms in the Indian Ocean, *Geophys. J. Int.*, **202**(2), 1180–1189.
- Dougherty, R.P. & Stoker, R.W., 1998. Sidelobe suppression for phased array aeroacoustic measurements, in *Proceedings of the 9th AIAA/CEAS Aeroacoustics Conference*, American Institute of Aeronautics and Astronautics Meeting Papers, pp. 235–245.
- Essen, H.-H., 2003. On the generation of secondary microseisms observed in northern and central Europe, *J. geophys. Res.*, **108**(B10), doi:10.1029/2002JB002338.
- Euler, G.G., Wiens, D. & Nyblade, A.A., 2014. Evidence for bathymetric control on the distribution of body wave microseism sources from temporary seismic arrays in Africa, *Geophys. J. Int.*, **197**(3), 1869–1883.
- Fäh, D., Stamm, G. & Havenith, H.B., 2008. Analysis of three-component ambient vibration array measurements, *Geophys. J. Int.*, **172**(1), 199–213.
- Featherstone, W., 1997. A novel method to improve the performance of Capon's minimum variance estimator, *Tenth International Conference on Antennas and Propagation (Conf. Publ. No. 436)*, IEE Conference Publisher, Vol 1, pp. 332–335.
- Friedrich, A., Klinge, K. & Krüger, F., 1998. Ocean-generated microseismic noise located with the Graefenberg array, *J. Seismol.*, **2**(1), 47–64.
- Gal, M., Reading, A.M., Ellingsen, S.P., Koper, K.D., Gibbons, S.J. & Näsholm, S.P., 2014. Improved implementation of the fk and Capon methods for array analysis of seismic noise, *Geophys. J. Int.*, **198**(2), 1045–1054.
- Gal, M., Reading, A.M., Ellingsen, S.P., Gualtieri, L., Koper, K.D., Burlacu, R. & Tkalčić, H., 2015. The frequency dependence and locations of short-period microseisms generated in the Southern Ocean and West Pacific, *J. geophys. Res.*, **120**(8), 5764–5781.
- Gerstoft, P., Shearer, P.M., Harmon, N. & Zhang, J., 2008. Global P, PP, and PKP wave microseisms observed from distant storms, *Geophys. Res. Lett.*, **35**(23), 1–6.
- Gibbons, S.J., Schweitzer, J., Ringdal, F., Kväerna, T., Mykkeltveit, S. & Paulsen, B., 2011. Improvements to seismic monitoring of the European Arctic using three-component array processing at SPITS, *Bull. seism. Soc. Am.*, **101**(6), 2737–2754.
- Hasselmann, K., 1963. A statistical analysis of the generation of microseisms, *Rev. Geophys.*, **1**(2), 177–210.
- Högbom, J., 1974. Aperture synthesis with a non-regular distribution of interferometer baselines, *Astron. Astrophys. Suppl. Ser.*, **15**, 417–426.
- Huestis, S., Molnar, P. & Oliver, J., 1973. Regional S_n velocities and shear velocity in the upper mantle, *Bull. seism. Soc. Am.*, **63**(2), 469–475.
- Jurkevics, A., 1988. Polarization analysis of three-component array data, *Bull. seism. Soc. Am.*, **78**(5), 1725–1743.
- Kelly, E.J., 1967. Response of seismic signals to wide-band signals, *Lincoln Lab. Tech. Note*, **30**, 1–46.
- Kennett, B. L.N., Stipčević, J. & Gorbato, A., 2015. Spiralarm seismic arrays, *Bull. seism. Soc. Am.*, **105**(4), 2109–2116.
- Koper, K.D. & Hawley, V.L., 2010. Frequency dependent polarization analysis of ambient seismic noise recorded at a broadband seismometer in the central United States, *Earthq. Sci.*, **23**, 439–447.
- Koper, K.D., Seats, K. & Benz, H., 2010. On the composition of Earth's short-period seismic noise field, *Bull. seism. Soc. Am.*, **100**(2), 606–617.
- Krim, H. & Viberg, M., 1996. Two decades of array signal processing research, *IEEE Signal Process. Mag.*, **13**(4), 67–94.
- Longuet-Higgins, M., 1950. A theory of the origin of microseisms, *Phil. Trans. R. Soc. Lond., A. Math. Phys. Sci.*, **243**(857), 1–35.

- Lucy, L.B., 1974. An iterative technique for the rectification of observed distributions, *Astron. J.*, **79**(6), 745, doi:10.1086/111605.
- Menon, R., Gerstoft, P. & Hodgkiss, W.S., 2014. On the apparent attenuation in the spatial coherence estimated from seismic arrays, *J. geophys. Res.*, **119**, 3115–3132.
- Ng, M.K., Chan, R.H. & Tang, W., 1999. A fast algorithm for deblurring models with Neumann boundary conditions, *SIAM J. Sci. Comput.*, **21**(3), 851–866.
- Nishida, K., Kawakatsu, H., Fukao, Y. & Obara, K., 2008. Background Love and Rayleigh waves simultaneously generated at the Pacific Ocean floors, *Geophys. Res. Lett.*, **35**(16), L16307, doi:10.1029/2008GL034753.
- Park, J., Lindberg, C. & Vernon, F., 1987. Multitaper spectral-analysis of high-frequency seismograms, *J. geophys. Res.*, **92**(B12), 12675–12684.
- Picozzi, M., Parolai, S. & Bindi, D., 2010. Deblurring of frequency–wavenumber images from small-scale seismic arrays, *Geophys. J. Int.*, **181**(1), 357–368.
- Poggi, V. & Fäh, D., 2010. Estimating Rayleigh wave particle motion from three-component array analysis of ambient vibrations, *Geophys. J. Int.*, **180**, 251–267.
- Reading, A.M., Koper, K.D., Gal, M., Graham, L.S., Tkalčić, H. & Hemer, M.A., 2014. Dominant seismic noise sources in the Southern Ocean and West Pacific, 2000–2012, recorded at the Warramunga Seismic Array, Australia, *Geophys. Res. Lett.*, **41**(10), 3455–3463.
- Richardson, W., 1972. Bayesian-based iterative method of image restoration, *J. acoust. Soc. Am.*, **62**(1), 55–59.
- Schimmel, M. & Gallart, J., 2003. The use of instantaneous polarization attributes for seismic signal detection and image enhancement, *Geophys. J. Int.*, **155**(2), 653–668.
- Schimmel, M. & Gallart, J., 2004. Degree of polarization filter for frequency-dependent signal enhancement through noise suppression, *Bull. seism. Soc. Am.*, **94**(3), 1016–1035.
- Schimmel, M., Stutzmann, E., Arduin, F. & Gallart, J., 2011. Polarized Earth's ambient microseismic noise, *Geochem. Geophys. Geosyst.*, **12**(7), doi:10.1029/2011GC003661.
- Schulte-Pelkum, V., Earle, P.S. & Vernon, F.L., 2004. Strong directivity of ocean-generated seismic noise, *Geochem. Geophys. Geosyst.*, **5**(3), doi:10.1029/2003GC000520.
- Sergeant, A., Stutzmann, E., Maggi, A., Schimmel, M., Arduin, F. & Obrebski, M., 2013. Frequency-dependent noise sources in the North Atlantic Ocean, *Geochem. Geophys. Geosyst.*, **14**(12), 5341–5353.
- Shepp, L.a. & Vardi, Y., 1982. Maximum likelihood reconstruction for emission tomography, *IEEE Trans. Med. Imaging*, **1**(2), 113–122.
- Shumway, R.H., Smart, E. & Clauter, D.A., 2008. Mixed signal processing for regional and teleseismic arrays, *Bull. seism. Soc. Am.*, **98**(1), 36–51.
- Sijtsma, P., 2007. CLEAN based on spatial source coherence, *Int. J. Aeroacoust.*, **6**(4), 357–374.
- Stephens, C. & Isacks, B.L., 1977. Toward an understanding of Sn: normal modes of Love waves in an oceanic structure, *Bull. seism. Soc. Am.*, **67**(1), 69–78.
- Traer, J., Gerstoft, P., Bromirski, P.D. & Shearer, P.M., 2012. Microseisms and hum from ocean surface gravity waves, *J. geophys. Res.*, **117**(B11307), doi:10.1029/2012JB009550.
- Vidale, J.E., 1986. Complex polarization analysis of particle motion, *Bull. seism. Soc. Am.*, **76**(5), 1393–1405.
- Wagner, G., 1996. Resolving diversly polarized, superimposed signals in three-component seismic array data, *Geophys. Res. Lett.*, **23**(14), 1837–1840.
- Wagner, G., 1997. Regional wave propagation in southern California and Nevada: observations from a three-component seismic array, *J. geophys. Res.*, **102**(B4), 8285–8311.
- Wagner, G. & Owens, T., 1996. Signal detection using multi-channel seismic data, *Bull. seism. Soc. Am.*, **86**(1A), 221–231.
- Wang, Y., Li, J., Stoica, P., Sheplak, M. & Nishida, T., 2004. Wideband RELAX and wideband CLEAN for aeroacoustic imaging, *J. acoust. Soc. Am.*, **115**(2), 757–767.
- Yardibi, T., Li, J., Stoica, P. & Cattafesta, L.N., 2008. Sparsity constrained deconvolution approaches for acoustic source mapping., *J. acoust. Soc. Am.*, **123**(5), 2631–2642.

SUPPORTING INFORMATION

Additional Supporting Information may be found in the online version of this paper:

Figure S1. (a) Illustration of zero padding of the original power spectrum (for ASAR). In this case we extend the image plane to $3N$ to account for the large extent of the used PSF. (b) Zero padded PSF of ASAR with an extent of $2N - 1$ pixels and normalised to unity volume. (c) Display of α where (b) is convolved with a mask object M_s to generate a field where the PSF mostly contributes to. (d) Shows w with a threshold parameter $\sigma = 0.09$.

Figure S2. Examples of different control parameters ϕ and their effect on the iteration process. The rings of constant velocity are set to 3.3 and 4.1 km/s.

Figure S3. Same as Fig. 3 but with a SNR of -20 dB and Hann window applied for ASAR only. The rings of constant velocity are set to 3.3 and 4.1 km/s.

Figure S4. Synthetic results for the case of extended sources. The columns show the 3 deconvolution algorithms and rows the 2 arrays. The rings of constant velocity are set to 3.3 and 4.1 km/s.

Figure S5. Illustrative figure for the case of 3 point sources, where each source is recorded by a single component only. The rings of constant velocity are set to 3.3 and 4.1 km/s.

Figure S6. Observed data results for ASAR for different iterations numbers and their power removal history. The power of the main peak is gradually reduced with increasing M as sidelobe contributions which overestimate the source power are removed. After iteration 600 scattering in (i) is visible which suggest that removed power may not be accurate. The rings of constant velocity are set to 3.3 and 4.1 km/s.

Figure S7. We show a Backazimuth histogram of removed power by the CLEAN algorithm. The synthetic configuration is identical to the case in Fig. 3. For the control parameter we select $\phi = 0.1$ and CLEAN iteration is stopped once 98 per cent of the synthetic power is removed. The red dots symbolise the true backazimuth and the true source power in decibel. (a) Shows 10 synthetic sources with a velocity < 3.715 km/s and (b) shows the remaining 3 sources with velocities > 3.715 . (c,d) Show the the same parameters but for CLEAN-PSF-Capon. The combined power for each source derived from the CLEAN approaches can be found in Table S2.

Figure S8. Same as Fig. S7, but for WRA. Beam power results for each source are shown in Table S3.

Figure S9. Same as Fig. S7, but for NORSAR. Beam power results for each source are shown in Table S3.

Table S1. Parameter of sources evaluated with the 3 component beamformer.

Table S2. Beam power for the synthetic test with the two CLEAN variations on ASAR. These values are derived from Fig. S7, by summing over a small backazimuth range for each source. Source 8 and 9 could not be separated and their power is displayed as the combined power over both backazimuth ranges. Iteration stopped after ~ 98 per cent of power was removed by CLEAN.

Table S3. Same as Table S2, but for WRA and NORSAR. The results are generated from Fig. S8 and Fig. S9. Iteration stopped after ~ 98 per cent of power was removed by CLEAN. (<http://gji.oxfordjournals.org/lookup/suppl/doi:10.1093/gji/ggw150/-/DC1>).

Please note: Oxford University Press is not responsible for the content or functionality of any supporting materials supplied by the authors. Any queries (other than missing material) should be directed to the corresponding author for the paper.

APPENDIX A: CLEAN-PSF-CAPON

The Capon beamformer can be formulated as the following minimisation

$$\min \mathbf{w}^\dagger \mathbf{C}(f) \mathbf{w} \quad (\text{A1})$$

under the constrain that the gain in the look direction \mathbf{k} is constant

$$\mathbf{w}^\dagger \mathbf{a}(\mathbf{k}) = 1. \quad (\text{A2})$$

The minimisation can be solved with the Lagrangian multiplier method and yields the weight vector

$$\mathbf{w} = \frac{\mathbf{C}^{-1}(f) \mathbf{a}(\mathbf{k})}{\mathbf{a}^\dagger(\mathbf{k}) \mathbf{C}^{-1}(f) \mathbf{a}(\mathbf{k})}. \quad (\text{A3})$$

Inserting into eq. (2) leads to the Capon beamformer (Capon 1969)

$$\mathbf{P}(\mathbf{k}) = \frac{1}{\mathbf{a}^\dagger(\mathbf{k}) \mathbf{C}^{-1}(f) \mathbf{a}(\mathbf{k})}. \quad (\text{A4})$$

CLEAN-PSF can be implemented by removing phase information from the cross-spectral matrix \mathbf{C} prior to its inversion. The algorithm can be summarised with the following steps (for a normalised steering vector $\mathbf{a}(\mathbf{k})$):

- (i) Calculate cross-spectral matrix \mathbf{C} , eq. (1).
- (ii) Compute the inverse \mathbf{C}^{-1} .
- (iii) Compute Capon beamformer, eq. (A4), and locate maximum in slowness plane.
- (iv) Remove fraction of power from cross-spectral matrix, $\mathbf{C}_{\text{PSF}}^{i+1} = \mathbf{C}^i - \phi P_{\text{Capon,max}}^i \mathbf{a}_{\text{max}} \mathbf{a}_{\text{max}}^\dagger$.
- (v) Place removed power into clean spectrum, eq. (6).
- (vi) Iterate steps (ii)–(v).
- (vii) Combine clean and background spectrum.

APPENDIX B: CLEANING EACH COMPONENT SEPARATELY WITH CAPON CLEAN-PSF-3C

The Capon beamformer in 3C is obtained by projecting the three orthogonal steering vectors onto the inverse cross-spectral matrix

$$\mathbf{Y}_{3\text{C,Capon}} = \mathbf{e}^\dagger(\mathbf{k}) \mathbf{C}_{3\text{C}}^{-1}(f) \mathbf{e}(\mathbf{k}). \quad (\text{B1})$$

Contrary to the conventional beamformer case, the power is given as

$$P_{3\text{C,Capon}}(\mathbf{k}) = \frac{1}{\lambda_0(\mathbf{k})} + \frac{1}{\lambda_1(\mathbf{k})} + \frac{1}{\lambda_2(\mathbf{k})}, \quad (\text{B2})$$

with $\lambda_0 > \lambda_1 > \lambda_2$. In this case, λ_2 is connected to the strongest polarisation. To clean each component separately we use the following steps:

- (i) Calculate cross-spectral matrix $\mathbf{C}_{3\text{C}}$, eq. (14), and create two additional duplicates.
- (ii) Compute the three inverse matrices $\mathbf{C}_{3\text{C},i}^{-1}$.
- (iii) Calculate three polarisation covariance matrices $\mathbf{Y}_{3\text{C},i}(\mathbf{k}) = \mathbf{e}^\dagger(\mathbf{k}) \mathbf{C}_{3\text{C},i}^{-1}(f) \mathbf{e}(\mathbf{k})$.
- (iv) Compute power for the two lowest eigenvalues and each component, $i = z, r, t$, $P_{3\text{C},i} = \sum_{n=1,2} \frac{1}{\lambda_{n,i}(\mathbf{k})} |\tilde{u}_{n,i}(\mathbf{k})|^2$ and find maximum in each component.
- (v) Remove fraction of power from 3C cross-spectral matrices, $m = z, r, t$, $\mathbf{C}_{3\text{C},m}^{i+1} = \mathbf{C}_{3\text{C},m}^i - \phi \sum_{j=1,2} \frac{1}{\lambda_{j,m}(\mathbf{k})} \mathbf{g}_j(\mathbf{k}) \mathbf{g}_j^\dagger(\mathbf{k})$.
- (vi) Place removed power into clean spectra, $P_{3\text{C,CLN},m}(\mathbf{k}) = \sum_i^M \phi P_{3\text{C,max},m}^i$.
- (vii) Iterate steps (ii)–(vi).
- (viii) Combine clean and background spectra.